Geoscience Letters

RESEARCH Open Access

Estimating crustal thickness in the northern Philippines: insights from ambient noise autocorrelation and receiver function analysis

Emi Ulfiana[1,2,4], Po-Fei Chen[2*], Bor-Shouh Huang[3], Cong-Nghia Nguyen[3] and Teresito C. Bacolcol[5]

Abstract

The Philippine archipelago comprises accreted terranes, including ophiolites, island arcs, and continental fragments. It absorbs the approximately 9 cm/year convergence between the Sundaland Plate to the west and the Philippine Sea Plate to the east. Understanding the crustal thickness variations across the Philippines is crucial for distinguishing collision boundaries and comprehending the complexities of tectonic evolution. In this study, we conducted ambient noise autocorrelation combined with receiver function analysis to estimate crustal thickness in the northern Philippines. To resolve ambiguities in the PmP phase in autocorrelation signals, Moho depth information from receiver function was utilized. We successfully identified coherent signals of PmP autocorrelation from 20 vertical seismograms, with two-way travel time ranging from 6.64 s to 13.79 s. These times correspond to crustal thicknesses of 19.8 to 46.0 km, respectively, as derived from the average CRUST1.0 P-wave velocity model. Our main findings and interpretations indicate that the crust beneath Luzon is slightly thicker in the western regions compared to the eastern parts. This suggests a limited influence of magmatic processes in the latter. Furthermore, our observations identified a tear in the slab at 17°N and 14°N latitude, characterized by thinner crust. We observed that the crust beneath Mindoro thickens in proximity to the collision of the microcontinental fragments with Mindoro-Panay island, whereas it thins toward the extension of the Pleistocene Macolod Corridor rifting.

Keywords Ambient noise autocorrelation, Crustal thickness in the northern Philippines, Macolod Corridor

Introduction

The Philippine archipelago is situated at the junction of the Sundaland Plate to the west and the Philippine Sea Plate to the east with a 9 cm/year convergence rate (DeMets et al. 2010). The high relative convergence is accommodated by two oppositely dipping subduction zones: the Manila Trench to the west and the East Luzon Trough–Philippine Trench systems to the east. Additionally, the major left-lateral strike-slip Philippine Fault, which traverses the length of the archipelago, plays a critical role in accommodating the oblique convergence between the plates (Karig 1983; Fitch 1972). Tectonically, the region comprises two major terranes: the Philippine Mobile Belt (PMB) and the Palawan Continental Block (PCB). The seismically active PMB consists of accreted terranes of ophiolite, island arcs, and continental fragments, whereas PCB is a microcontinental fragment of Eurasia that rifted off due to the opening of the South China Sea (Karig 1983). This complex tectonic history is

*Correspondence:
Po-Fei Chen
bob@ncu.edu.tw
[1] Taiwan International Graduate Program (TIGP) - Earth System Science Program (ESS), Academia Sinica and National Central University, Academia Sinica, Taipei, Taiwan
[2] Department of Earth Sciences, National Central University, Taoyuan, Taiwan
[3] Institute of Earth Sciences, Academia Sinica, Taipei, Taiwan
[4] Indonesian Agency for Meteorology Climatology and Geophysics (BMKG), Jakarta, Indonesia
[5] Department of Science and Technology, Philippine Institute of Volcanology and Seismology, Quezon, Philippines

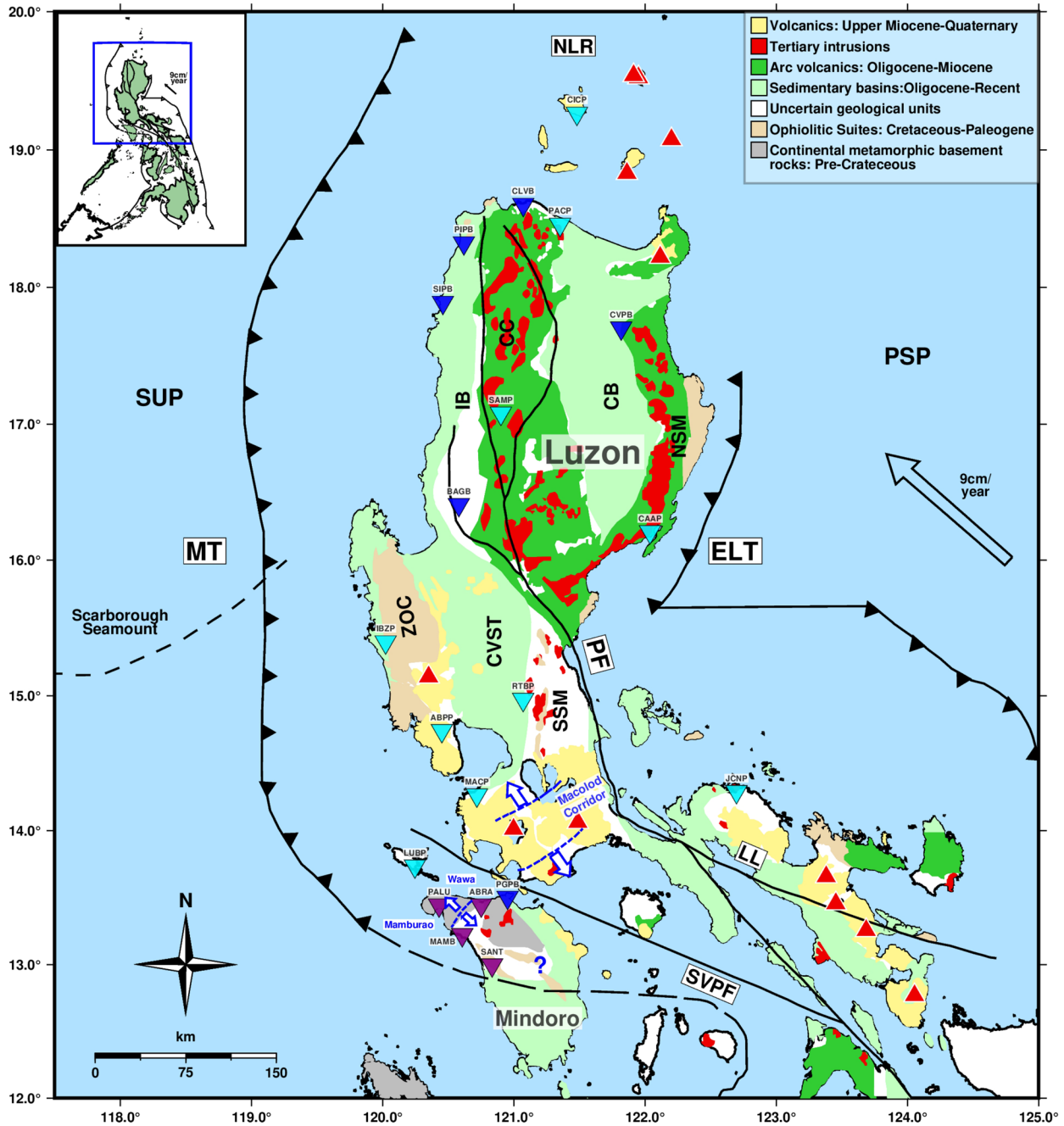

Fig. 1 Tectonic and geological setting in the northern Philippines. Geological terranes are adapted from Zhang et al. (2020) and are explained in the legend. The relative motion between the Philippines Sea Plate (PSP) and the Sundaland Plate (SUP) is indicated by a black arrow. The Manila Trench (MT), East Luzon Trough (ELT), and Philippine Trench (PT) are represented by saw-toothed lines pointing in the direction of subduction. The major Philippine Fault System (PF), Sibuyan Verde Passage Fault (SVPF), and Legaspi Lineament (LL) are shown as solid lines. The black dashed lines represent the Scarborough Seamount Chain Blue dashed lines with arrow illustrate the Macolod Corridor rifting zone and its westward extension toward Wawa and Mamburao in Mindoro (Chen et al. 2015). A black dashed line in central Mindoro indicates the hypothesized collision boundary between the Palawan Continental Block (PCB) and the Philippine Mobile Belt (PMB) (Yumul et al. 2009). Red triangles indicate active volcanoes. Inverted triangles represent station locations, with colors indicating data sources: blue (Institute of Earth Sciences, Academia Sinica-IES), sky blue (Philippine Institute of Volcanology and Seismology-PHIVOLCS), and brown (National Central University-NCU). NLR: North Luzon Ridge; IB: Ilocos Basin; CC: Cordillera Central; CB: Cagayan Basin; NSM: Northern Sierra Madre Range; ZOC: Zambales Ophiolite Complex; CVST: Central Valley Suture; SSM: Southern Sierra Madre Range

reflected in the present-day structure of the Philippines (Fig. 1).

In the northern Philippines, two principal islands are included: Luzon entirely within the PMB, and Mindoro with portions belonging to both PMB and PCB. In Luzon, a slab tear occurred at about 16 to 17°N and 17.5°N as a result of subduction of the Scarborough seamount chain, an indicator of an extinct Mid Oceanic Ridge (MOR) beneath Luzon island, west of the Manila trench (Bautista et al. 2001; Fan et al. 2014; Nguyen et al. 2023). The geological complexity of Luzon is further emphasized by the identification of at least half a dozen terranes, including the North and Central Luzon Terranes (Karig 1983). South of Luzon, these western Luzon terranes are juxtaposed with Mindoro, where an arc–continent collision occurred between the PCB and PMB, with the Manila trench terminating at approximately 13°N (McCabe et al. 1982). Yumul et al. (2009) indicated the collision boundary traverses central Mindoro. The collision has resulted in significant tectonic features, including the formation of a pull-apart rift zone within the Macolod Corridor and slab tearing near 14°N (Bautista et al. 2001; Bina et al. 2020).

The crustal composition exhibits significant variation in the northern Philippines, complicating the interpretations of the subsurface configuration. Understanding the subsurface structure is essential for constructing tectonic models and relates directly to the region's geology and tectonic history. Furthermore, crustal structure information is crucial for earthquake location analysis and plays a key role in seismic hazard assessments. This understanding can be advanced by estimating the crustal thickness variation through the identification of the Mohorovičić discontinuity (Moho), the boundary between the Earth's crust and upper mantle. Over the years, crustal thickness in the Philippine arc has been estimated using various methods: gravity modeling (e.g., Manalo et al. 2015; Parcutela et al. 2020), seismic receiver function beneath Tagaytay seismic station (Besana et al. 1995), and geochemical data (Plank and Langmuir 1988; Dimalanta and Yumul 2003). While gravity and geochemical methods provide valuable insights, seismic wave analysis remains the most reliable approach for studying crustal seismic boundaries. By observing reflected and refracted seismic waves at contrasting velocity boundaries, high-resolution results can be achieved (Grad et al. 2009)

We derive the autocorrelation function (ACF) of ambient noise—a zero-offset seismic Green's function reflection method—combined with receiver function analysis. We collected the data from 20 vertical seismic stations in the northern Philippines, including Luzon, Mindoro, and two smaller interspersed islands: Lubang (LUBP) and Calayan Island (CICP, Fig. 1). Our analysis revealed a thicker crust within the Luzon terranes compared to Mindoro, where significant crustal thickening is observed near the collision boundary. Additionally, areas of crustal thinning are associated with slab tearing beneath the region or the extension of the Macolod Corridor.

Accreted terranes in the northern Philippines

The geological complexity of Luzon is characterized by at least six distinct terranes (Fig. 1). In the Northern Luzon Terranes, these include the Ilocos Basin (IB), Cordillera Central (CC), Cagayan Basin (CB), and Northern Sierra Madre Range (NSM). In Central Luzon, the terranes include the Eocene Zambales Ophiolite Complex (ZOC) and Southern Sierra Madre Range (SSM) which are separated by Central Valley Suture (CVST), a suture zone marking the boundary between accreted crustal blocks (Karig 1983). The CC is the longest mountain range in the Philippines, separating the IB to the west and the CB to the east. It is a magmatic arc formed by subduction along the Manila Trench during the early Miocene, with peaks reaching up to 3000 m (Bellon and Yumul 2000). The Sierra Madre of eastern Luzon represents the remains of an east-facing arc and is composed of large dioritic complexes emplaced in a thick Late Cretaceous–Paleocene sequence of mafic volcanic units. These units overlie a sialic basement, and the entire package has been thrust eastward over the oceanic crust, suggesting westward subduction during the Early Cenozoic (De Bour et al. 1980). The SSM is separated from the NSM by the active Philippine Fault. The ZOC extends from Lingayen Gulf to Subic Bay. In the south, the western Luzon terranes are adjacent to the Mindoro metamorphic basement block, which has been colliding with the northern part of the PCB since the Miocene (Karig 1983).

Method

Autocorrelation of ambient noise

The autocorrelation of ambient noise allows us to determine the zero-offset Green's functions beneath seismic stations through seismic interferometry, where a single station acts as both the source and the receiver (Snieder et al. 2009). The powerful ACF tool requires neither earthquake nor man-made sources. The groundwork for this seismic noise interferometry approach was laid by Aki (1957) through the spatial autocorrelation method (SPAC), demonstrating the feasibility of studying the local subsurface without requiring source information. This approach was further developed by Claerbout (1968), who identified the autocorrelation of a transmitted plane wave with normal incidence propagating through a layered medium and showed how it could be used to infer the reflection response of the medium. Wapenaar et al. (2010) elaborated on the principles

Table 1 List of 20 stations used in this study

Sta	Autocorrelation function (ACF)				Receiver function (RF)				Criteria
	N	Bandpass filter (Hz)	TWT of PmP (s)	TWT to depth (km)	Moho depth (km)	*Vp/Vs*	Total events	Events selected	
CICP	3	0.25–1.5	6.64 ± 0.3	19.8 ± 0.89	19.7 ± 1.24	1.77 ± 0.123	19	6	C
CLVB	6	0.8–2.0	9.64 ± 0.34	28.5 ± 1.01	31.7 ± 1.3	1.82 ± 0.073	106	16	C
PACP	6	1.3–2.5	9.87 ± 0.36	29.2 ± 1.06	31.5 ± 1.29	1.9 ± 0.083	27	17	A
PIPB	8	0.5–1.5	10.75 ± 0.58	32.5 ± 2.58	33.8 ± 2.82	1.60 ± 0.095	82	9	A
SIPB	7	0.5–2.0	10.11 ± 0.37	29.8 ± 1.17	32.5 ± 2.70	1.78 ± 0.124	71	16	C
SAMP	6	1.3–2.5	9.1 ± 0.22	26.9 ± 0.65	26.2 ± 2.42	2.02 ± 0.125	31	17	C
BAGB	7	0.5–1.5	10.6 ± 0.4	32 ± 1.78	34.8 ± 1.53	1.68 ± 0.077	121	22	C
IBZP	6	1.0–2.0	9.5 ± 0.74	28 ± 2.19	30.9 ± 3.45	1.9 ± 0.144	33	14	B
ABPP	6	1.3–2.5	10.07 ± 0.58	29.8 ± 1.75	29.6 ± 1.4	1.59 ± 0.102	15	7	A
MACP	4	0.5–1.5	10.41 ± 0.48	31 ± 2.13	26.9 ± 2.77	2.06 ± 0.223	31	18	C
CVPB	6	0.6–2.0	9.45 ± 0.67	27.9 ± 1.98	–	–	–	–	B
CAAP	6	0.8–1.7	9.76 ± 0.52	28.9 ± 1.54	29.0 ± 2.24	1.84 ± 0.113	26	19	C
RTBP	6	0.7–1.8	8.9 ± 0.18	26.4 ± 0.53	26.7 ± 1.55	1.70 ± 0.087	32	27	C
JCNP	4	1.0–2.0	10.67 ± 0.54	32 ± 2.11	29.3 ± 1.56	1.97 ± 0.089	29	15	A
LUBP	3	1.3–2.5	7.36 ± 0.34	21.8 ± 1.01	21.7 ± 3.37	1.75 ± 0.266	35	7	B
PALU	8	0.5–2.0	7.89 ± 0.37	23.3 ± 1.09	28.4 ± 1.70	2.00 ± 0.097	99	28	B
ABRA	3	0.5–2.5	9 ± 0.27	26.6 ± 0.8	31.7 ± 1.73	1.98 ± 0.130	50	7	C
PGPB	4	0.5–2.0	9.55 ± 0.78	28.3 ± 2.31	32 ± 1.5	1.87 ± 0.084	105	9	C
MAMB	7	0.5–2.5	8.1 ± 0.3	24.1 ± 0.89	–		–	–	B
SANT	5	0.5–1.5	13.79 ± 1.01	46 ± 4.49	40.6 ± 2.79	1.60 ± 0.063	31	6	A

Sta denotes the station name. *N* represents the number of months in the data period. Each station has a different stacking duration due to variations in data quality and availability. The bandpass filter is adjusted individually for each station. TWT of PmP refers to the two-way travel time of PmP (in seconds) and its corresponding depth conversion. Moho Depth is derived from Receiver Function analysis. *Vp/Vs* is the ratio of P- to S-wave velocities, calculated using the *H-κ* method. Total events and Events selected indicate the number of earthquakes before and after quality control in the receiver function analysis. Criteria represents the confidence level of the results, as explained in the Results section

underlying 3D reflected wave interferometry, illustrating how individual receivers could be treated as virtual sources to extract reflected body waves from ambient noise and thereby image Earth's structure. Several studies have successfully applied body wave interferometry to detect reflected body waves from Moho discontinuity (e.g., Ruigrok et al. 2011; Gorbatov et al. 2013).

The data for this study consist of continuous 1-day records collected from 20 vertical broadband stations (Fig. 1) established through collaborate on between the Philippine Institute of Volcanology and Seismology (PHIVOLCS), the Institute of Earth Science (IES) at Academia Sinica, and National Central University (NCU). The duration of each station used in autocorrelation ranges from 3 to 8 months (Table 1), depending on the availability and quality of the data.

ACF processing is divided into two phases: (1) data preparation and ACF computation, followed by (2) stacking and phase analysis (Fig. 2). In the first phase, the continuous 24-h raw data are segmented into 1-h windows. Preprocessing involved removing the mean to center the data around zero, applying trend removal, and using a

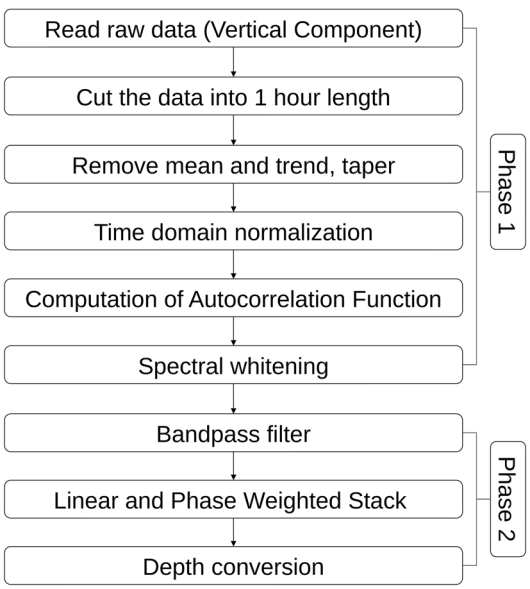

Fig.2 The workflow of this study is segmented into two phases: Phase 1 involves data preparation and autocorrelation function (ACF) computation, while Phase 2 focuses on stacking and phase analysis

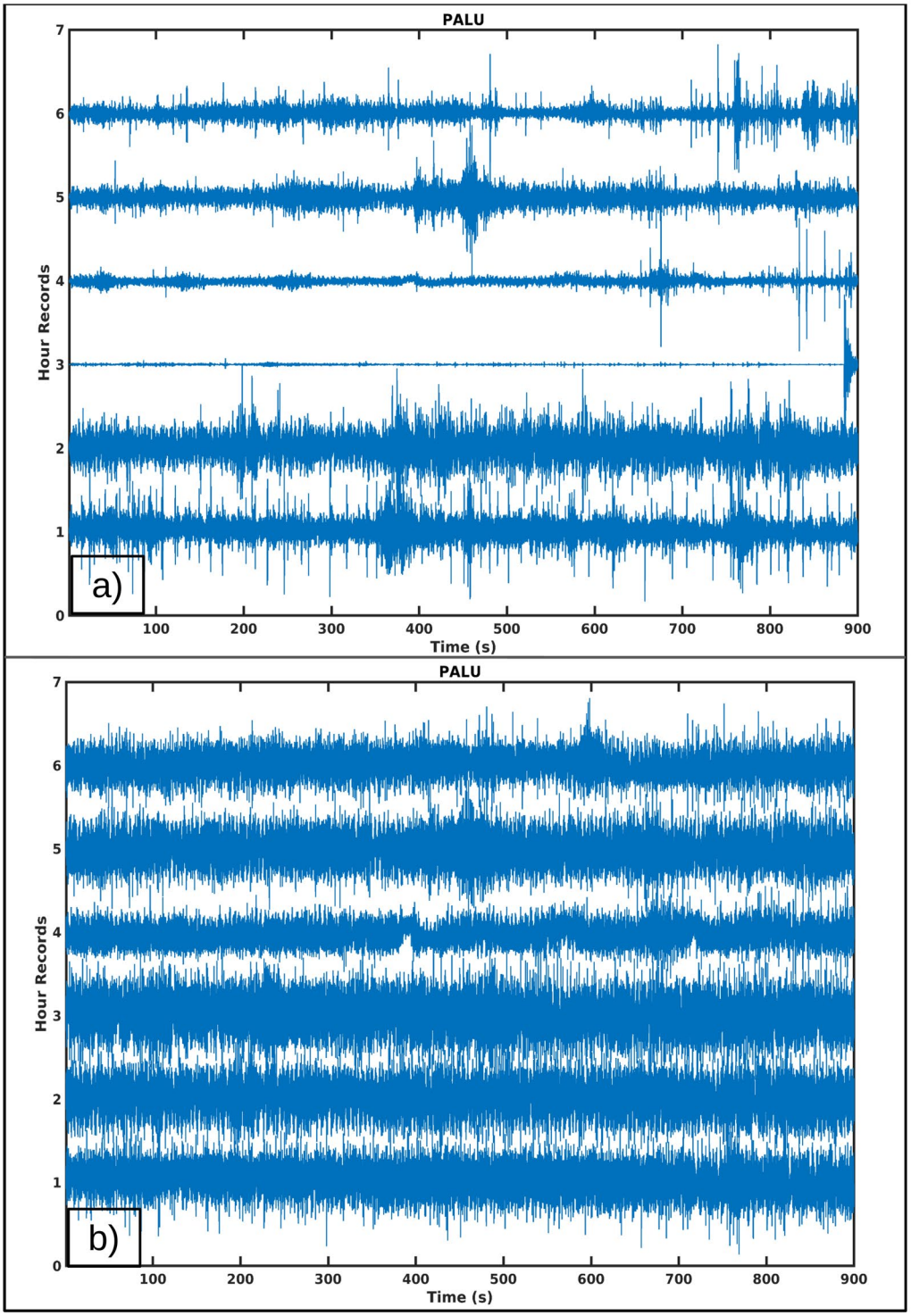

Fig. 3 **a** The raw data after mean removal, detrending, and tapering. Each 15-min segment is part of six 1-h ambient noise recordings retrieved from station Palu on May 2, 2019, between 00;00 and 06;00 (UTC). **b** The same data as in (**a**) after applying temporal normalization using the running absolute mean method with a window size of 90 points

Tukey window for the tapering function. Time-domain normalization was implemented using running absolute mean (Bensen et al. 2007) to reduce the impacts of earthquakes, instrumental inconsistencies, and non-stationary noise sources near the stations. Figure 3 shows the 15-min time windows extracted from six 1-h segments of preprocessed data recorded by station PALU on May 2, 2019, along with the same data after time-domain normalization. Spectral whitening was applied to minimize the effects of primary and secondary microseismic sources (Bensen et al. 2007; Oren and Nowack 2016). Additionally, we applied a $\frac{\pi}{2}$ phase shift correction to account for contributions from teleseismic sources to the stationary phase in ACF (Gómez-García et al. 2022; Morcjek and Tilmann 2021).

In the second phase, an appropriate bandpass filter was applied to each station to isolate a clear and reliable PmP phase, highlighting the most prominent reflectors at the Moho Discontinuity (Fig. S2), as the ACF is frequency-dependent (Kennett 2015). To ensure positive reflection phase amplitude, the ACF was multiplied by −1. The artifacts between 0 and 5.5 s are muted to enhance the visibility of the reflection phase, excluding the largest pulse around $t=0$ s (Fig. 4). Hourly ACFs were stacked into daily records, which were further aggregated using both linear and non-linear phase-weighted stack (PWS; Schimmel and Paulssen 1997) over several months. The two-way travel time (TWT) was converted to depth through the average 1D CRUST 1.0 P-wave velocity model (Fig. S1; Laske et al. 2013) to estimate the Moho depth (Fig. 5). CRUST1.0 was selected due to its applicability and availability of consistent velocity and thickness parameters across the study area. While CRUST1.0 provides consistent coverage, we also tested regional 1D and 3D models from Nguyen et al. (2023), which yielded Moho depths 4–13 km deeper than those from CRUST1.0, highlighting the sensitivity of depth conversion to the choice of velocity model. Nevertheless, CRUST1.0 was retained for its simplicity and overall agreement with RF-derived depths.

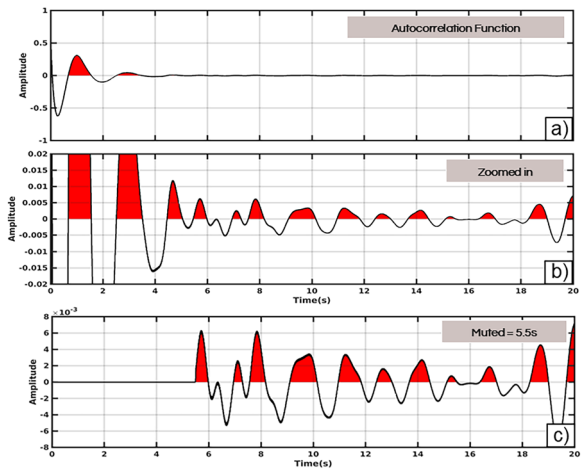

Fig.4 **a** The casual part of the linear stacked ACF recorded at station PALU was shifted by π/2 and multiplied by −1. The 20 s of the ACF show a strong energy peak at zero lag time. **b** A zoomed-in view of (**a**), illustrating the PmP phase arrival at approximately 8 s. **c** The same ACF after muting the first 5.5 s, which enhances the clarity of the PmP arrival near 8 s

In PWS computation, the linear stack is weighted by the coherency of its instantaneous phase, reducing incoherent noise and enhancing weak coherent signals, as defined in Eq. (1). The $g(t)$ is the product of the real part of the seismic trace $S_j(t)$ and its instantaneous phase $\Phi_k(t)$ with the weight of ν. Consequently, if ν is set to zero, the result will be equivalent to the linear stack. For all stations, we applied a phase-weighting exponent of $\nu = 2$, as it sufficiently reduces contributions from non-stationary phases without overly diminishing weaker signals:

$$g(t) = \frac{1}{N}\sum_{j=1}^{N} S_j(t)\left|\frac{1}{N}\sum_{k=1}^{N}\exp[i\Phi_k(t)]\right|^{\nu}. \quad (1)$$

Based on the coherence of instantaneous phase, we evaluated the ACF picks computation and systematically assessed the reliability of PmP phase. Phase coherence was plotted as a function of lag time, focusing on the 6–14 s window (approximately 10 ± 4 s), where PmP reflection phase is expected to occur. We identified the two most prominent coherence peaks and calculated their difference of amplitude maxima. Based on the difference, ACFs were classified into two categories. Grade A (high confidence) was assigned when the difference exceeded 0.1 (Fig. 6a, b), indicating that the first coherence maximum phase corresponds to a clear PmP phase. In contrast, Grade B (ambiguous) was defined by a difference ≤ 0.1 (Fig. 6c), requiring additional corroboration from RF computation. In order to better quantify pick uncertainty, we calculated the width at 10% of the highest coherence amplitude, which was used to define the uncertainty of TWT and Moho depth.

Receiver function of teleseismic earthquakes

Receiver function analysis complements ACF by providing sensitivity to phases associated with Moho discontinuity. This technique focuses on *P*–*S* conversion at the interface beneath the recording station. The teleseismic receiver function represents the structural response near a recording station by deconvolving the source time function of the incoming teleseismic *P*-waves. The $H-\kappa$ (crustal thickness—*Vp*/*Vs*) method (Zhu and Kanamori

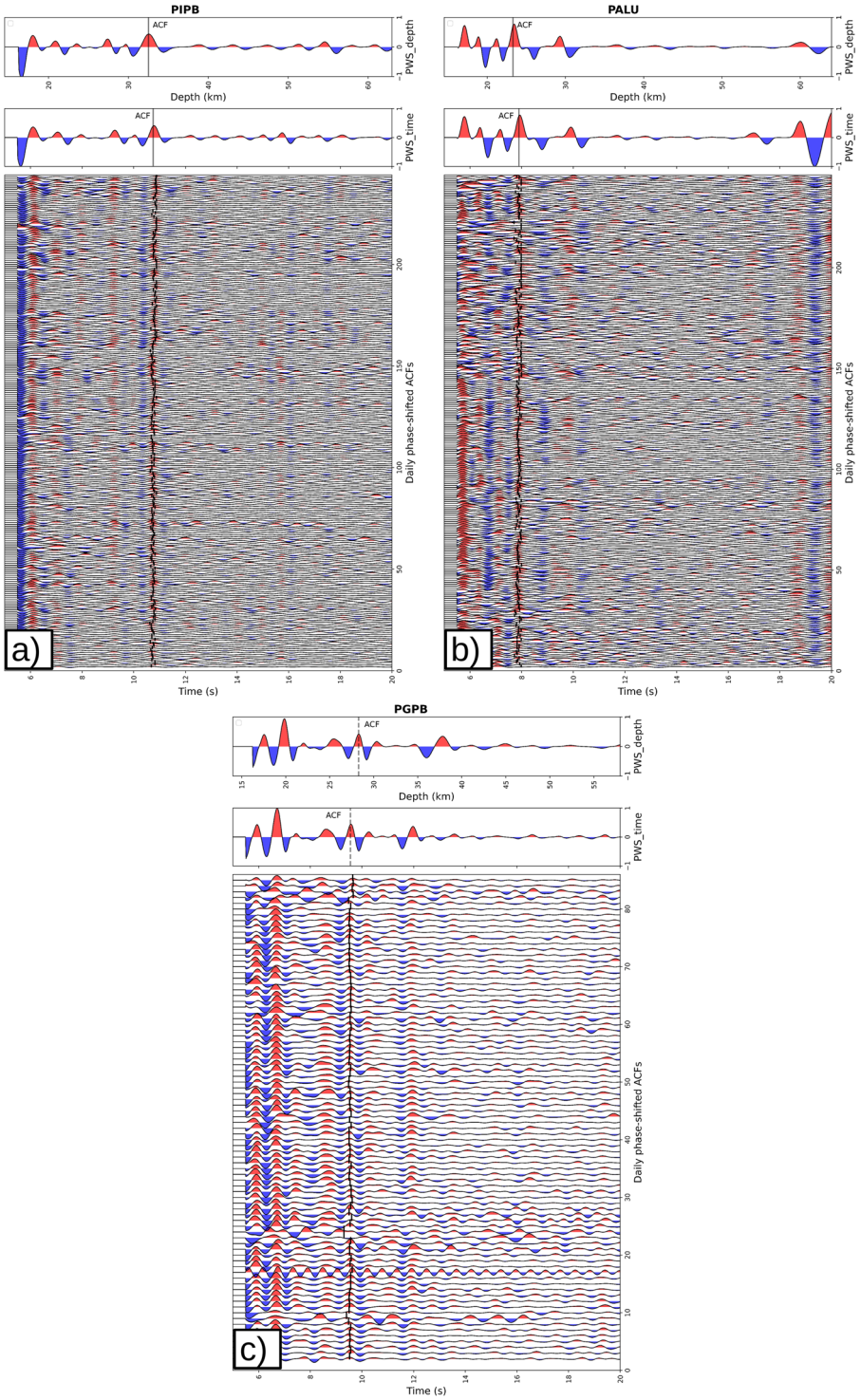

Fig. 5 **a** Daily stack of ACF over 20 s (bottom), and 8-month phase-weighted stacks in the time and depth domains (middle and top panels, respectively) for station PIPB. **b** Same as (**a**) but for station PALU. The PmP phases are clearly identified and unambiguous, as also evidenced by their coherence in Fig. 6a, b; both stations are classified as Grade A in the ACF analysis. **c** Same as (**a**) and **b**, but for station PGPB, using three months of data. This station is classified as Grade B, as multiple possible PmP phases are identified

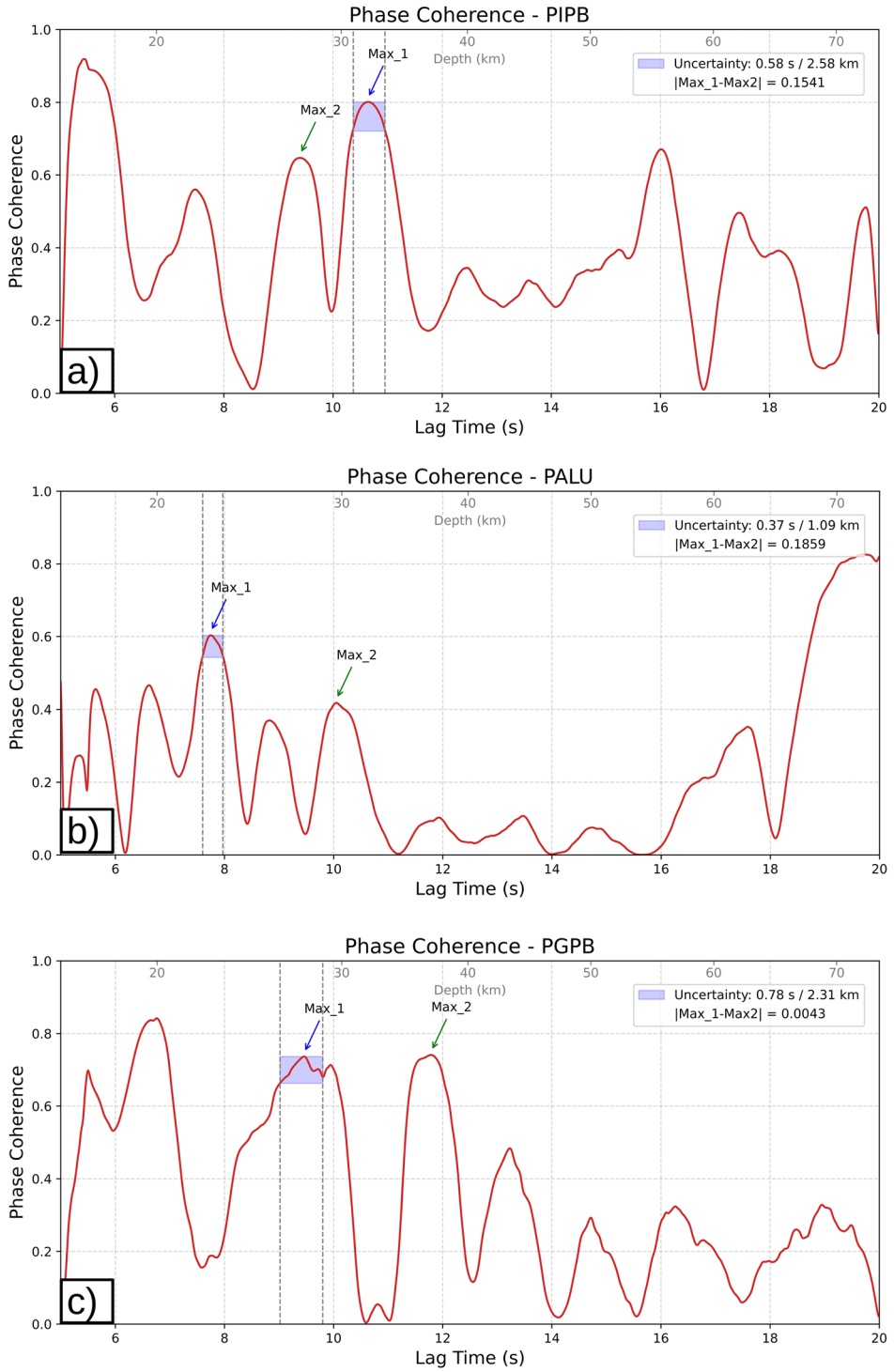

Fig.6 The coherence terms for stations PIPB (**a**), PALU (**b**), and PGPB (**c**). **a** and **b** Are classified as Grade A (high confidence), showing a distinct difference between the first and second of amplitude maxima (> 0.1). **c** Is classified as Grade B, exhibiting an ambiguous PmP pick (difference ≤ 0.1). Dashed lines indicate the uncertainty interval, defined as the range where the coherence amplitude drops to 90% of its maximum value

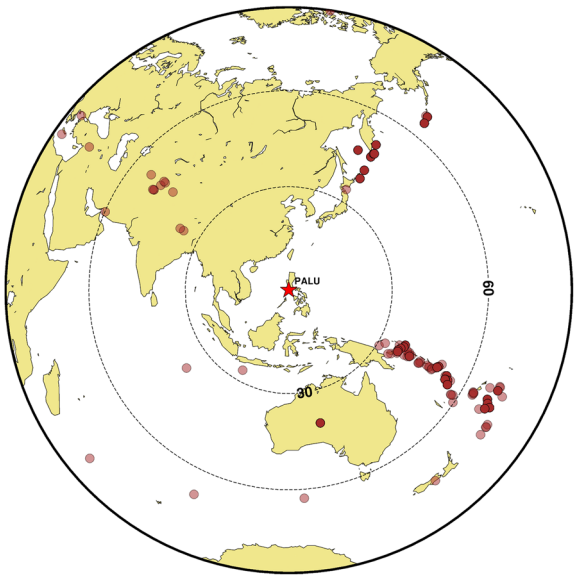

Fig. 7 Teleseismic earthquakes (brown circles) with magnitude M ≥ 5.5 recorded by station PALU between 2013 and 2017. Earthquakes used to compute receiver function at station PALU are shown in transparent brown. The star marks the location of station PALU. Dashed lines indicate distances at 30° intervals from the station

2000) was implemented using Seispy, a Python package by Xu and He (2022).

Eighteen stations were included in the analysis (Table 1), excluding CVPB, where the first arrival of the reference P-wave was not distinctly detectable and was shifted from zero time; and MAMB, where the horizontal components were not properly recorded. The selection criteria for teleseismic earthquake data included epicentral distances of 30°–90° and magnitudes above M 5.5 (Fig. 7). Due to limited data availability, only a few earthquakes were processed for receiver function analysis (Table 1). A bandpass filter of 0.05–2.0 Hz was applied with a signal-to-noise ratio (SNR) threshold of 0.7. Waveforms were rotated from NS–EW–vertical to transverse–radial–vertical (TRZ), followed by Gaussian filter and water-level deconvolution (Clayton and Wiggins 1976; Ammon 1991). Figure 8 illustrates the R–T component for stations PIPB, PALU, and PGPB based on back-azimuth. In the R component, the *Ps* phase is the most prominent phase following the P-wave, reflecting the large velocity contrast at the crust–mantle boundary. The RFs for all stations are presented in Figure S3.

Crustal thickness (H) for *Ps* phase can be estimated using Eq. (2). Vp and Vs represent the P and S-wave velocities, p is the ray parameter or horizontal slowness (s/km), and t_1 is the arrival time of *Ps* phase (s). The P-wave velocity (Vp) is adopted from the average of 1D CRUST1.0. The crustal thickness is strongly dependent on Vp/Vs. A 0.1 variation in Vp/Vs may introduce a change in crustal thickness of approximately 4 km (Zhu and Kanamori 2000). To further reduce the ambiguity, we include the multiples (i.e., *PpPs* and *PsPs* + *PpSs*) in addition to *Ps* to provide additional constraints (Eqs. 3, 4):

$$H = \frac{t_1}{\sqrt{\frac{1}{V_s^2} - p^2} - \sqrt{\frac{1}{V_p^2} - p^2}}, \tag{2}$$

$$H = \frac{t_2}{\sqrt{\frac{1}{V_s^2} - p^2} + \sqrt{\frac{1}{V_p^2} - p^2}}, \tag{3}$$

$$H = \frac{t_3}{2\sqrt{\frac{1}{V_s^2} - p^2}}, \tag{4}$$

$$s(H,\kappa) = w_1 r(t_1) + w_2 r(t_2) - w_3 r(t_3). \tag{5}$$

We acknowledge that the multiples are sometimes weak or incoherent across stations due to a lack of data, dipping layers, and/or anisotropy effects. It is well established that crustal anisotropy and/or dipping Moho interfaces can introduce significant biases in Moho depth and Vp/Vs estimates from RF analysis (Levin and Park 1997; Cassidy 1992). The effects of anisotropy of a single dipping Moho are simulated (Figs. S4 and S5) and stacked to produce synthetic receiver functions (Fig. S6). We conclude that the influence of dip becomes particularly pronounced at dip angles exceeding 15°, where the amplitudes of the multiple phases broaden and exhibit increased delay compared to the flat Moho scenario. In the T component, higher dip angles generate stronger amplitudes for both the converted Ps and the multiple phases. The Ps phase itself remains relatively stable in both amplitude and arrival time, even at dip angles up to 20°. The effects of Moho dip on H–κ stacking were systematically examined by Lombardi et al. (2008), showing that for typical continental crust (20–40 km thick) with dip ≤ 5°, the Moho depth bias remains < 1 km smaller than the true value. However, for Moho depths > 40 km and dip > 10°, the H–κ stacking method can underestimate the true depth by at least 3 km and up to 6 km for Moho depths 70–80 km.

In several cases, we observed indications of crustal anisotropy or dipping layers, represented by coherent energy on the T component and incoherent signals for some azimuth in the R component (Bai et al. 2010; Savage 1998), as exemplified by station PALU (Fig. 8b). We note that the presence of multiple phases with lower and broader amplitudes suggests that significant Moho dip may not be pervasive in our dataset, or at least not severe enough to fully obscure the multiples. Therefore, we retained the

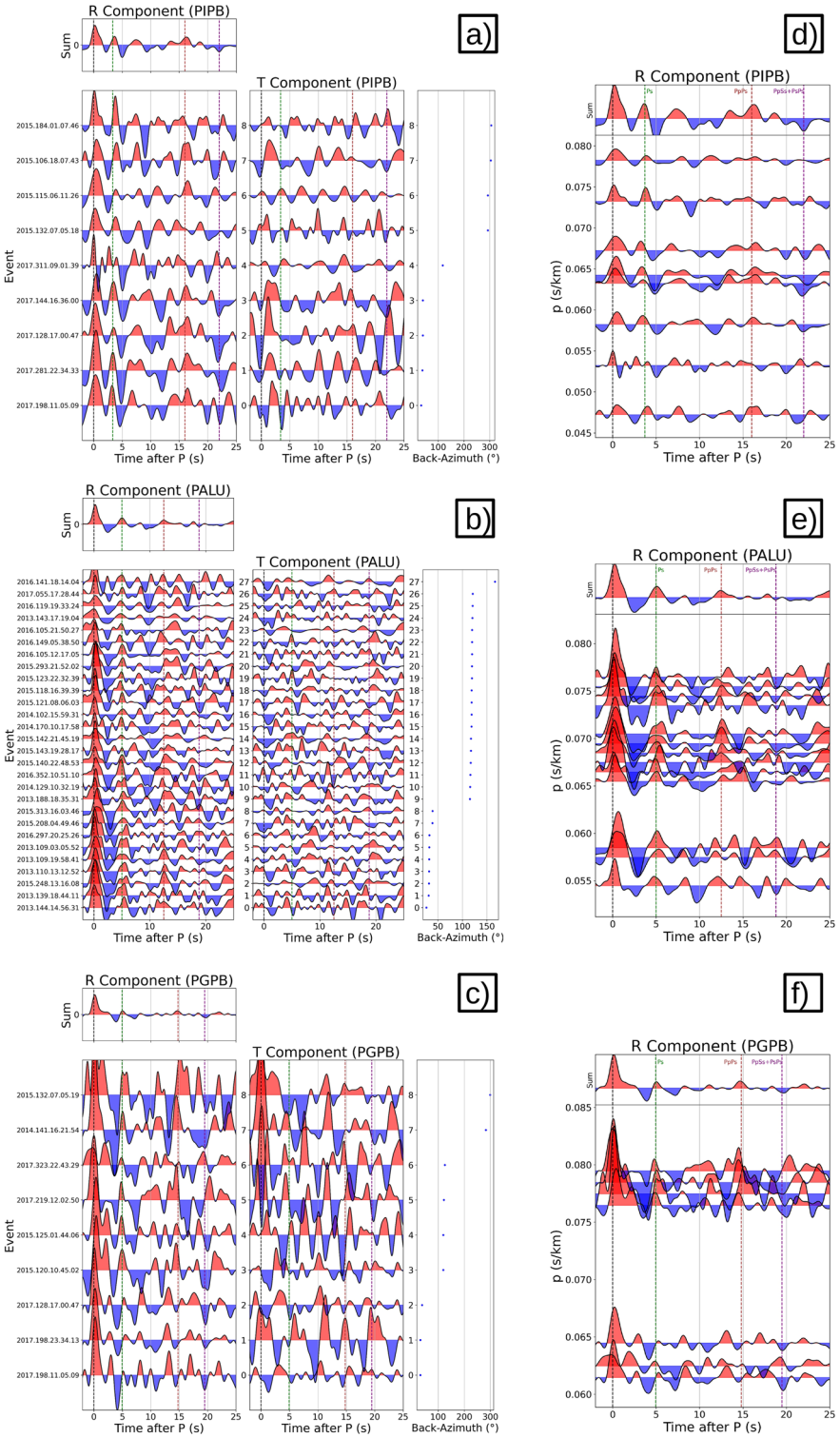

Fig. 8 **a** Radial and transverse (R–T) components of receiver functions for station PIPB, sorted by back-azimuth, showing clear multiple phases. **b** Same as (**a**), but for station PALU. The multiples are not coherent and exhibit broader stacked amplitudes, indicating the presence of a dipping layer. **c** Same as (**a**), but for station PGPB, showing clear multiples. **d**–**f** R component sorted by ray parameter (p) for station PIPB, PALU, and PGPB, respectively. The green, brown, and purple dashed lines represent the arrival time of Ps, PpPs, and PsPs + PpSs phases, respectively

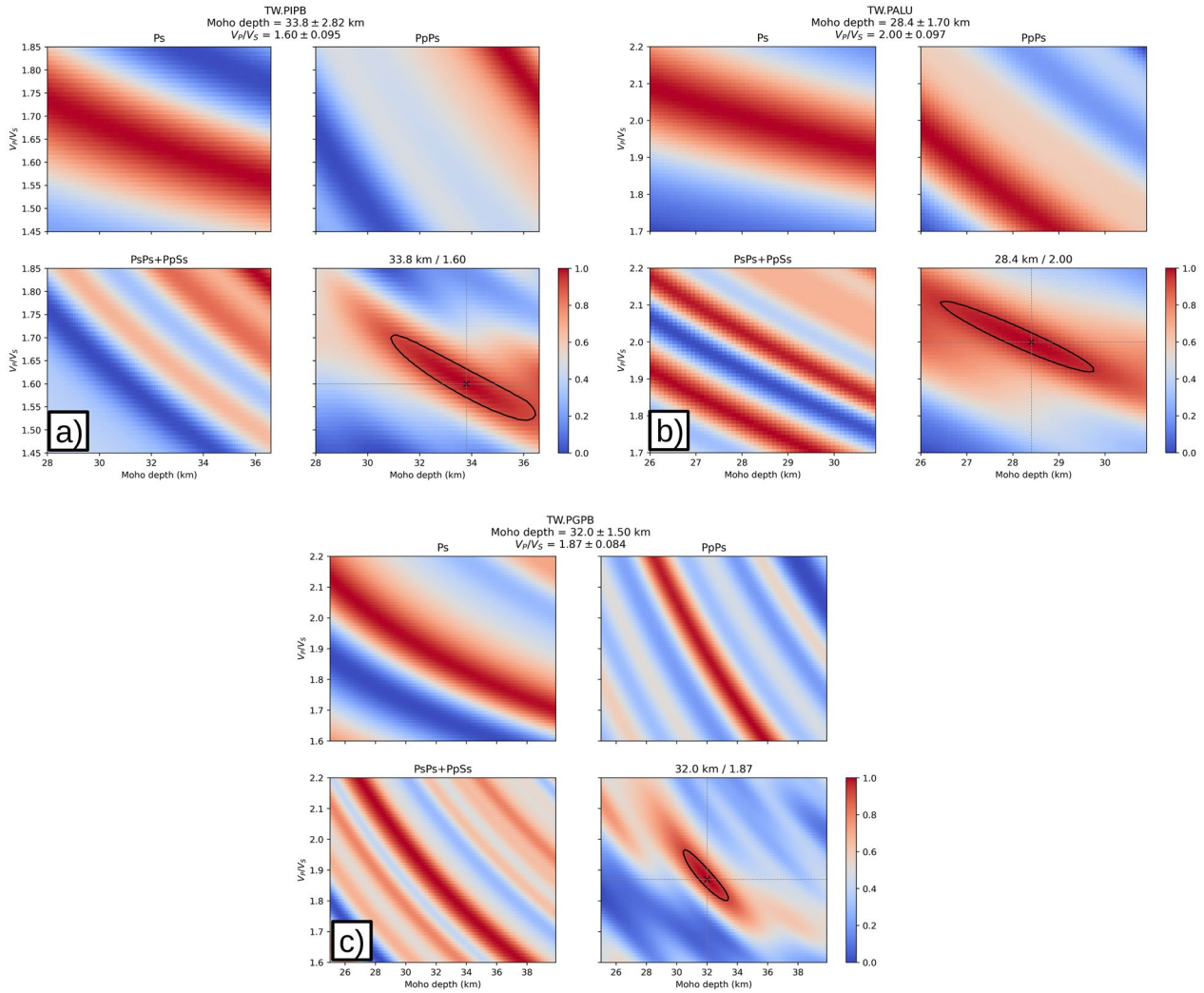

Fig. 9 Moho depth estimation from Ps, PpPs, PsPs + PpSs phases using receiver function analysis at stations PIPB (**a**), PAL (**b**), and PGPB (**c**). The black cross marks the location of the maximum stacking amplitude, and the black ellipse represents the confidence level contour

H-*κ* stacking results but applied lower weights to weak amplitude phases. In addition, we treated the RF results as auxiliary constraints when interpreting the PmP with ambiguous ACF signals. We recognize that our current approach to resolving anisotropy and dipping interfaces has limitations.

In Eq. (5), the different weightings (w) of each phase in the radial receiver function (r) were applied for stacking, based on their normalized stacking amplitude. Specifically, w_1, w_2, and w_3 correspond to the weights for *Ps*, *PpPs*, and *PsPs* + *PpSs*, respectively. For each phase, we calculate the stacking amplitude and normalize it such that the total sum of weights satisfies $\Sigma w_i = 1$. This adaptive weighting ensures that stronger, more coherent phases are assigned a greater contribution in the H–κ estimation, while weaker phases are down-weighted (Figs. S7 and S8, Table S1).

The maximum stacking $_{s(H,\kappa)}$ is achieved when all phases are stacked coherently. To visually verify the predicted arrival times of *Ps* and its multiples, we provided RFs according to the ray parameter p (Fig. 8). For example, at station PALU (Fig. 8e), the stacking of 27 receiver functions resulted in a crustal thickness H of 28.4 km with κ of 2.00 (Fig. 9b), consistent with the predicted strong converted *Ps* arrival time at 5.0 s after the initial *P*-wave arrival. The confidence contour surrounding the stacking maxima (Fig. 9) is calculated based on the 1-standard deviation interval of the stacking values, as $c = 1 - \frac{\sigma_s}{\sqrt{N}}$, where σ_s is the standard deviation of the stacking function and N is the number of events. The

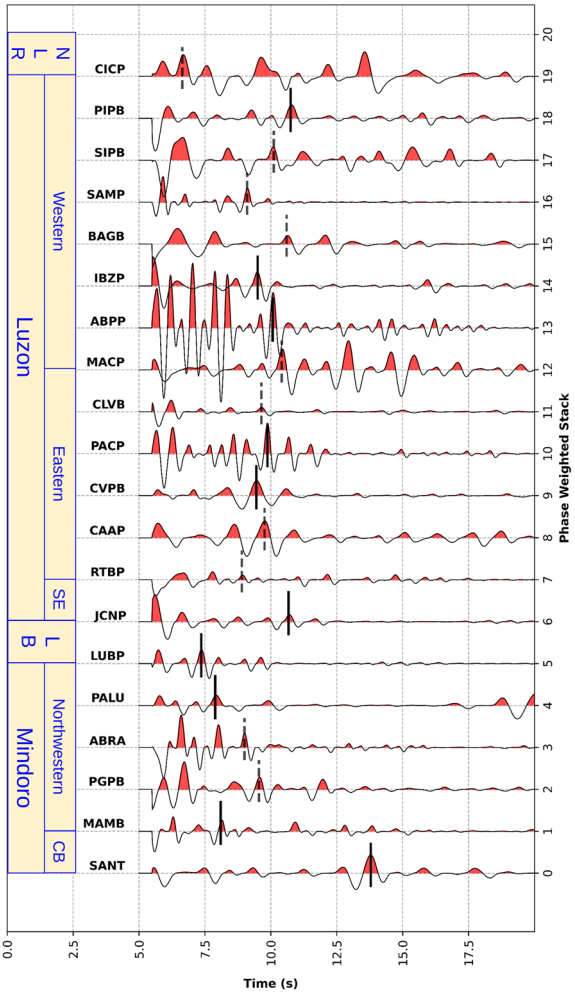

Fig. 10 Two-way travel time for all stations. The black solid and dashed lines indicate the PmP arrival with high and low confidence pick levels (i.e., Grade A and B). The ACFs are multiplied by –1 to obtain the PmP at positive amplitude. NLR: North Luzon Range, SE: Southeastern Luzon, LB: Lubang Island, CB: collision boundary

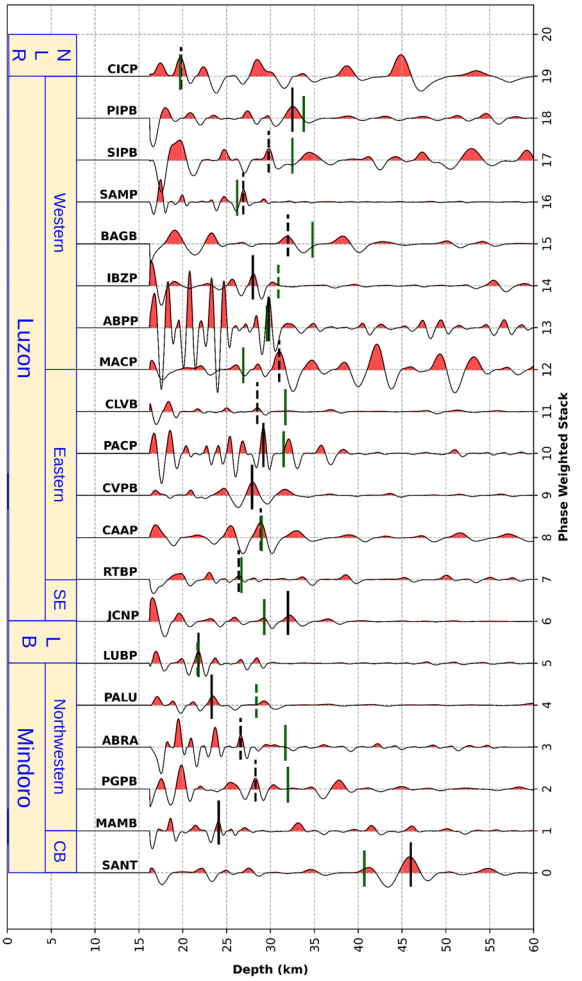

Fig. 11 Depth conversion through CRUST1.0 based on Fig. 10. The black and green lines represent the Moho depth derived from the autocorrelation function and receiver function, respectively. Solid lines indicate high-confidence levels, while dashed lines denote low-confidence levels. Abbreviations are as defined in Fig. 10

uncertainties in H and κ are estimated by taking half the difference between their maximum and minimum values along the confidence contour (i.e., $\sigma_H \approx (H_{\max} - H_{\min})/2, \sigma_\kappa = (\kappa_{\max} - \kappa_{\min})/2$). We evaluated the RF results based on visual inspection of multiple phases clearance and the Moho depth uncertainty, and subsequently grouped the RFs into two categories. Grade A (high confidence) includes RFs that exhibit clear multiples and Moho depth uncertainty ≤3km (Figs. 8a, c, 9a, c). Grade B (lower confidence) comprises RFs with weak multiples and/or Moho depth uncertainty > 3km (Figs. 8b, 9b).

Crustal thickness estimation

By combining the results of the ACF and RF methods, the reliability of the Moho depth is categorized into four criteria (Table 1):

Criteria A: both ACF and RF are classified as Grade A.

Criteria B: ACF is Grade A and RF is Grade B.

Criteria C: ACF is Grade B and RF is Grade A.

Criteria D: both ACF and RF are Grade B (this category is excluded from the final results).

In Figs. 10, 11, Grade A results are shown as solid lines, and Grade B as dashed lines. Black lines represent the ACF analysis, while green lines represent the RF analysis. For example, a green dashed line indicates a Grade B result from the RF method. For Criteria A, the ACF analysis provides the primary Moho depth, with the RF result serving as supporting evidence. For Criteria B, the Moho

depth is determined solely from the ACF result. The RF analysis offers only supplementary information due to issues such as weak multiple phases, depth uncertainty greater than 3 km, or the absence of reliable RF data. For Criteria C, the RF result serves as the primary constraint, guiding the selection of the PmP phase in the ACF analysis. In this case, the ACF picking is performed near the Moho depth indicated by the RF result.

Results

Autocorrelation function

The TWTs of PmP across all stations are presented in Table 1 and depicted in Fig. 10. In general, the PmP arrives earlier in Mindoro compared to Luzon, where the western region of Luzon exhibits longer PmP travel times than the eastern region. The average TWT of PmP in Luzon and Mindoro (excluding SANT station) is 9.91 ± 0.59 s and 8.64 ± 0.78 s, respectively. Within Luzon, the area south of the North Luzon Ridge records the earliest PmP arrivals with a TWT of 6.64 s at CICP, located at Calayan Island. In the northwestern tip of Luzon, two stations situated in the IB, on the western flank of the CC Cenozoic magmatic arc—PIPB and SIPB—have TWTs of about 10 s. The stations located within the CC-CLVB, PACP, SAMP, and BAGB—exhibit TWTs of 9.64 s, 9.87 s, 9.10 s, and 10.6 s, respectively. In the eastern part of Northern Luzon terranes, within the CB and NSM Range, the TWTs at stations CVPB and CAAP are 9.45 s and 9.76 s, respectively. In the central Luzon terranes, stations IBZP and ABPP located within the ZOC record TWTs of 9.50 s and 10.07 s, respectively. South of ZOC, station MACP, located near the rifting zone of the Macolod Corridor, records a TWT of 10.41 s. In the SSM, station RTBP records the earliest TWT at 8.9 s. Further southeast in Luzon, within the Bicol arc, station JCNP records a TWT of 10.67 s.

In Mindoro, station LUBP, located on Lubang Island NW of Mindoro, records the earliest TWT of PmP at 7.36 s. This is followed by stations in northern Mindoro, PALU and MAMB, with arrival times of 7.89 s and 8.1 s, respectively. In northwestern Mindoro, two nearby stations, ABRA and PGPB, record TWTs of approximately 9 s and 9.55 s. The latest PmP arrival is observed at station SANT, with a TWT of 13.79 s.

In a depth conversion (Fig. 11) the crust beneath the Luzon arc is generally thicker than that beneath Mindoro. The average crustal thickness in Luzon and Mindoro (excluding station SANT) is 29.45 ± 2.0 km and 25.58 ± 2.3 km, respectively. In the western Luzon arc, crustal thickness is approximately 30–32 km in the IB, 32 km in the southern CC, 28–31 km in the ZOC, and 31 km north of the rifting zone of Macolod Corridor. All these regions exhibit similar thicknesses. On the other hand, thinner crust is observed beneath the CC at station SAMP and the SSM at station RTBP, with Moho depths of 27 km and 26 km, respectively. In eastern Luzon, where the crust is generally thinner than in the west, the crustal thickness ranges between 28 and 29 km in the CB and NSM. In the southeastern Luzon region, specifically in Bicol arc, the only station JCNP shows a crustal thickness of 32 km. In Mindoro, Lubang Island—NW of Mindoro, has a crustal thickness of 22 km, relatively thinner than in other areas, followed by station PALU (23 km) and MAMB (24 km) in northwestern Mindoro. In the northeastern part of Mindoro, two nearby stations, ABRA and PGPB have crustal thicknesses of 27 km and 28 km, respectively. The thickest crust in Mindoro is observed at station SANT, with a thickness of 46 km.

Receiver function

Using receiver function analysis, the crustal thickness ranges from 20 to 35 km in Luzon and 22 km to 41 km in Mindoro (Fig. 11). Notably, a particularly thin crust of 20 km was identified at the North Luzon Ridge, while crustal thicknesses of 26 km and 27 km were observed at stations SAMP in the CC region and RTBP in the SSM, respectively. In the Northern Luzon Terranes, crustal thicknesses of 34 km and 32 km were observed beneath the IB at stations PIPB and SIPB, respectively. In the CC, crustal thickness ranged from 32 to 35 km, excluding station SAMP (26 km). Additionally, in the eastern part of the Northern Luzon terrane, the NSM exhibited a crustal thickness of 29 km. Within the central Luzon Terranes, crustal thickness ranged from 27 to 31 km, including 30–31 km beneath the ZOC and 27 km northwest of the rifting zone of the Macolod Corridor and in the SSM. In the southern Luzon Terrane, the only available station, JCNP, located in the Bicol region, recorded a crustal thickness of 29 km.

A relatively thin crust measuring 22 km was observed at station LUBP on Lubang Island. In Mindoro, a crustal thickness of 28 km was identified at station PALU. Similarly, the stations ABRA and PGPB exhibited nearly identical crustal thicknesses, measuring 31.7 km and 32.0 km, respectively. The thickest crust, 41 km, was observed at station SANT. Overall, the crustal thickness derived from the receiver function aligns well with measurements obtained using ambient noise autocorrelation, thereby corroborating the validity of the results.

We also analyzed the *Vp/Vs* using the *H-κ* stacking method (Table 1). The average *Vp/Vs* in Luzon is 1.82 ± 0.16, which is lower than the average *Vp/Vs* in NW Mindoro, 1.95 ± 0.07. Notably, areas associated with slab tearing, such as station SAMP, exhibit the highest *Vp/Vs* of 2.02 ± 0.125. Additionally, the high *Vp/Vs* (> 1.8) are observed beneath regions including the CC, the ZOC,

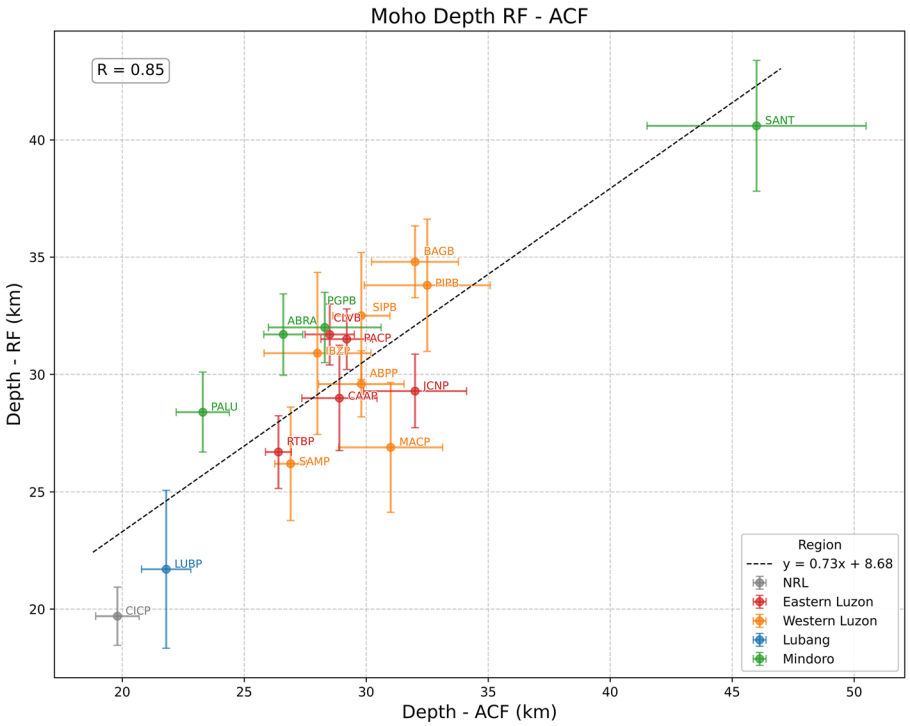

Fig. 12 Comparison of Moho depth estimates from the receiver function (RF) and the autocorrelation function (ACF). Data points are color-coded by station region, with station codes labeled accordingly. The linear trend indicates strong agreement between the two methods, with a correlation coefficient of 85%

the area NW of the rifting zone of Macolod Corridor, and Bicol. In Mindoro, most stations also exhibit high *Vp/Vs* values, except at the collision boundary, where a significantly lower *Vp/Vs* of 1.60 ± 0.063 is observed.

Consistency between ACF and RF

To illustrate the consistency between the two approaches, we plotted the Moho depth estimated from ACF and RF, as shown in Fig. 12. The horizontal and vertical error bars represent the uncertainty in Moho depth obtained from ACF and RF, respectively. In ACF, the Moho depth ranges from 19.8 ± 0.89 km to 46 ± 4.49 km, with associated uncertainties between ± 0.5 and 4.5 km. The Moho depth in RF ranges from 19.7 ± 1.24 km to 40.6 ± 2.79 km, with uncertainties between ± 1.2 and ± 3.4 km. The results of ACF and RF generally follow a linear trend, with RF depths being greater than ACF depths overall.

Significant discrepancies between the two methods that exceed the combined uncertainties $\left(\sqrt{\sigma_{\mathrm{ACF}}^2 + \sigma_{\mathrm{RF}}^2}\right)$ are observed at several stations. At MACP, the ACF depth is 4.1 km greater than RF depth, exceeding the combined uncertainty of ~ 3.4 km, likely associated with the rifting of the Macolod Corridor. Similarly, at SANT, the ACF depth is greater than the RF depth by 5.4 km, marginally larger than the combined uncertainty of ~ 5.3 km, possibly related to structural complexity near the PCB–PMB collision boundary. For other stations in Mindoro (PALU, ABRA, and PGPB), the ACF depths exhibit shallower depths than RF, with discrepancies of 5.1, 5.1, and 3.7 km, respectively. These discrepancies exceed the combined uncertainties of 2.0 km, 1.9 km, and 2.8 km, respectively. This may be attributed to the adoption of CRUST 1.0, which is more representative of the northern Philippines, as well as the influence of dipping interfaces and/or anisotropy (Figs. S4, S5, and S6).

Additionally, we provide the ACF and RF waveforms in Fig. 13 (station IBZP and SAMP). The signals demonstrate that the timing of PmP arrival in TWT of ACF and Ps-converted phase in RF are consistent and align closely with theoretical predictions. Specifically, the PmP arrives approximately ~ 9–10 s, which is about twice the arrival time of Ps at ~ 4–5 s. These observations are consistent with both phases corresponding to the same crustal discontinuity. This convergence reinforces the reliability of the inferred crustal thickness and the complementarity of the two methods.

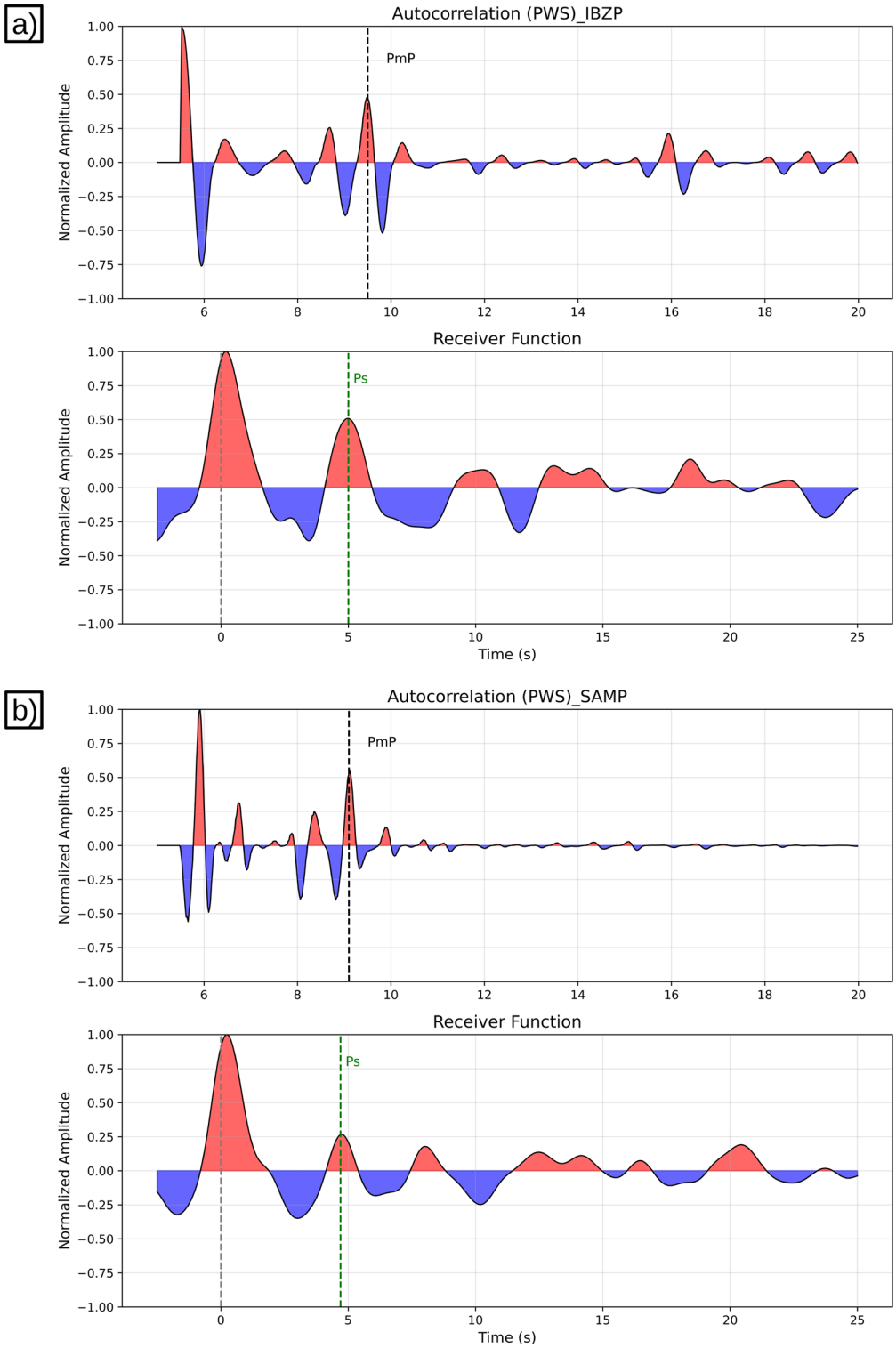

Fig. 13 **a** Phase-weighted stack of the autocorrelation function signal (top) and the radial component of receiver function (bottom) for station IBZP. The PmP and Ps arrivals are marked by dashed black and green vertical lines, respectively. **b** Same as **a**, but for station SAMP

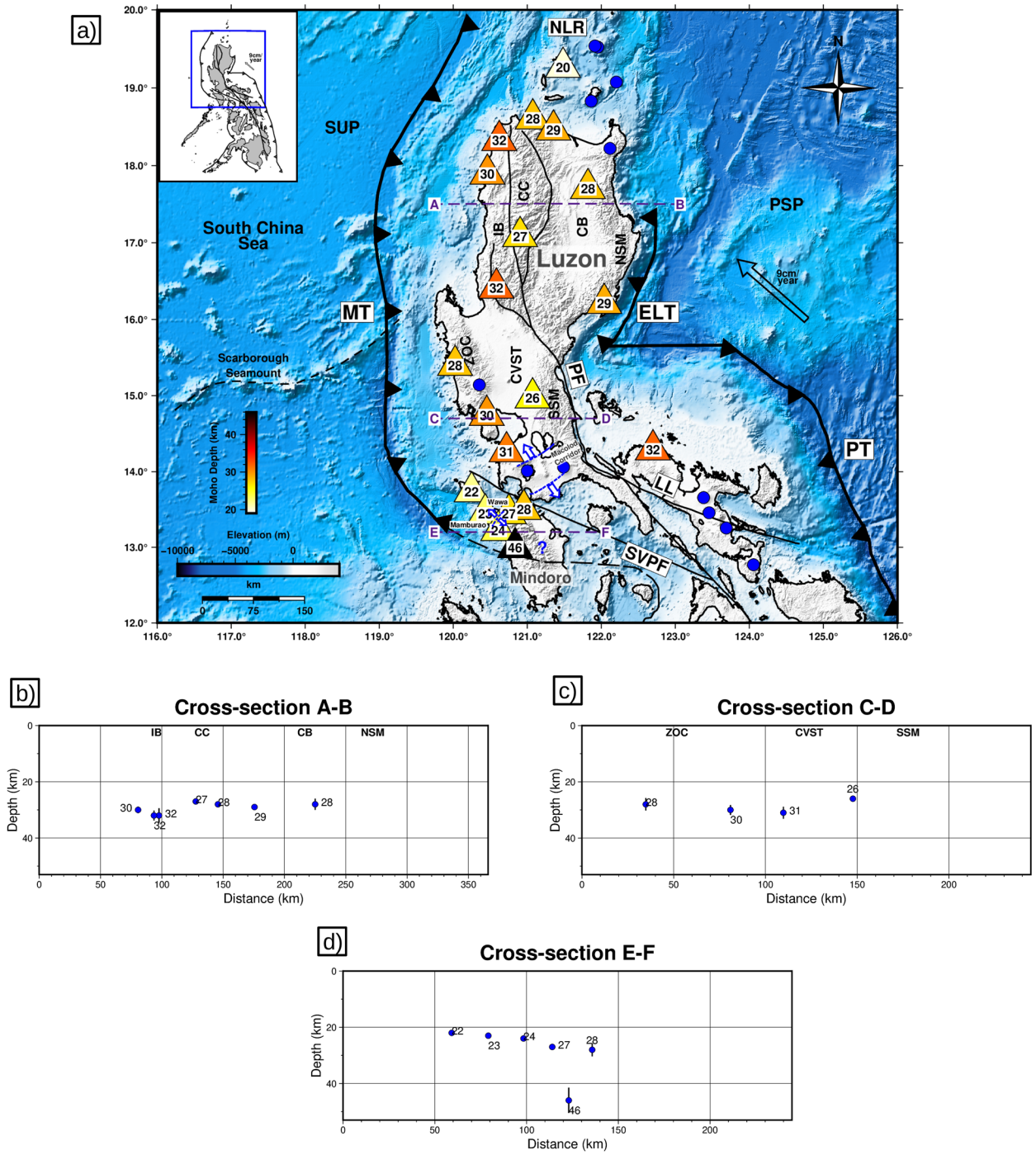

Fig. 14 **a** Moho depth distribution across the study area. The numbers indicate Moho depth estimates beneath each station. Abbreviations are as defined in Fig. 1. **b** Cross-section of Moho depth along profile AB, including stations within ± 1.3° latitude tolerance. **c**, **d** Same as (**b**), but for profiles CD and EF, with stations within ± 0.9° latitude tolerance

Discussion

Several geological processes contribute to crustal growth, including the emplacement of ophiolite and the magmatic process. In this study, we identified a crust significantly thicker than typical oceanic crust—approximately 20 km thick—within the Calayan Island arc, located south of the North Luzon Ridge (Fig. 14). The crustal shortening and thickening south of the North Luzon Ridge are attributed

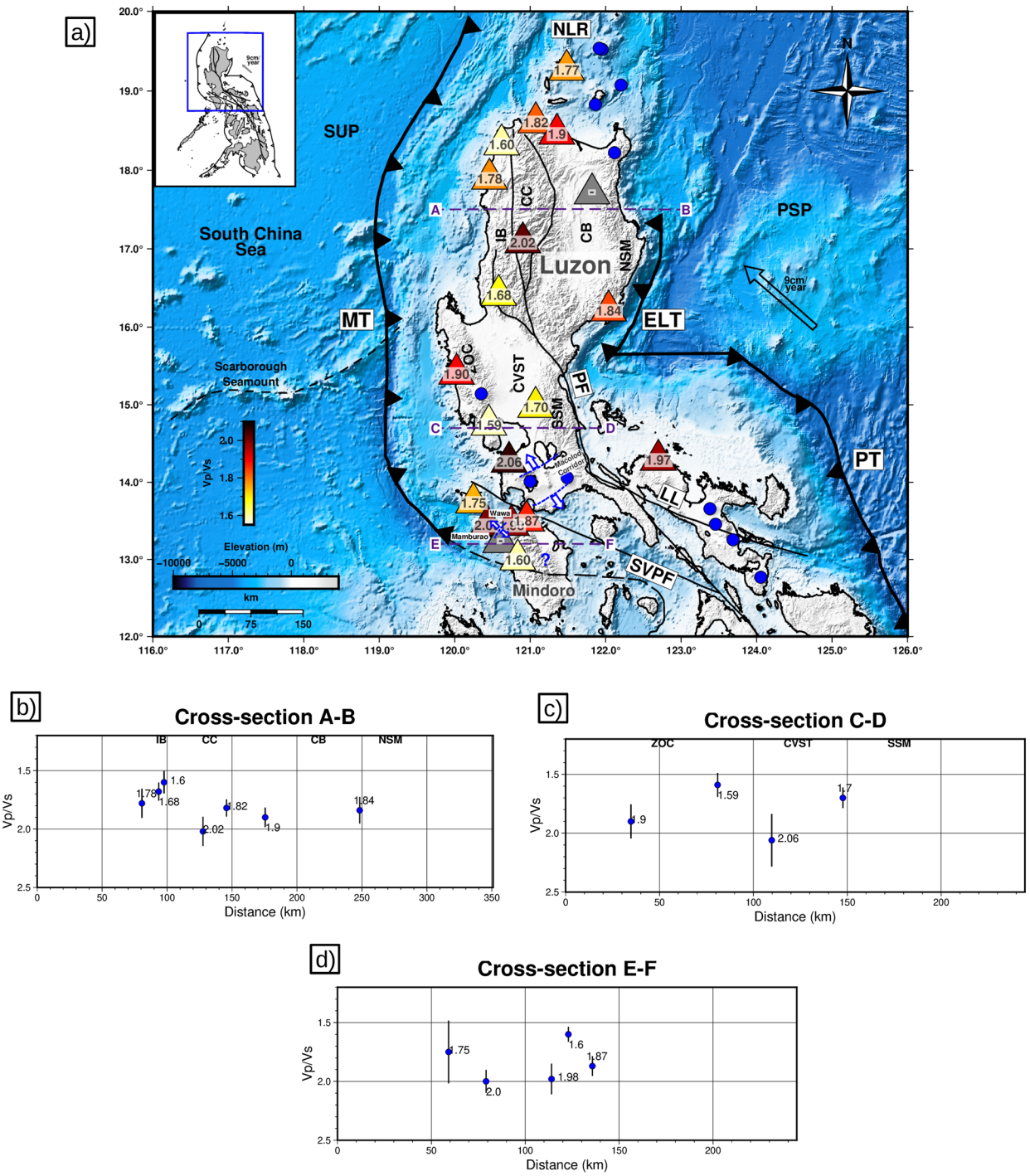

Fig. 15 **a** Vp/Vs ratio distribution across the study area. The numbers indicate the Vp/Vs at each station. Abbreviations are as defined in Fig. 1. **b** Cross-section of the Vp/Vs ratio along profile AB, including stations within ± 1.3° latitude tolerance. **c**, **d** Same as (**b**), but for profiles CD and EF, with stations within ± 0.9° latitude tolerance

to the initial phase of subduction along the East Luzon Trough and the Philippine Trench (Lewis and Hayes 1989; Bautista et al. 2001). In the northern Luzon block, the relatively thinner crust observed eastward from the IB to the NSM (Fig. 14b) may be due to the accumulation of more island arc materials in the western continental

terrane, while the subduction along the east commenced more recently, limiting the contribution of the magmatic process to the volume arc (Bautista et al. 2001; Karig 1983). South of CC, at approximately 17°N, the thinner crust at station SAMP can be related to the north–south extensionality of the overriding plate due to slab tearing, a result of the subduction of the MOR beneath Luzon (Bautista et al. 2001). Focal mechanisms in this region indicated shallow normal-faulting earthquakes at the outer trench, corresponding to a north–south extensional regime at crustal level, in contrast to the thrust faulting typically observed in the subducting slab (Nguyen et al. 2023). The highest *Vp/Vs* was observed in this area (Fig. 15), consistent with findings by Nguyen et al. (2023), who also identified low-velocity zones and high *Vp/Vs* in regions associated with the slab tearing at 16–17°N. These phenomena are attributed to high-temperature magmas rising through the slab window created by slab tearing.

In the central Luzon block, the thick crust is associated with the ZOC, potentially resulting from ophiolite emplacement via strike-slip faulting, which adds material to the crust. This region is also characterized by high free-air anomalies, suggesting it may be a southern extension of CC (Dimalanta and Yumul 2004). Crustal thickness and *Vp/Vs* in the CC and ZOC exhibit similar characteristics, with high *Vp/Vs*. South of ZOC, a 30 km thick crust beneath station ABPP was observed, along with low *Vp/Vs*. Nguyen et al. (2023) also identified P- and S-wave low-velocity anomalies in this region, likely linked to magmatic processes beneath the western volcanic chain due to subduction along the Manila Trench. The significantly large amplitude in the ACF at station ABPP might reflect local amplification related to the low-velocity structure beneath the volcano. In the northwest of the Macolod corridor rifting zone, the observed Moho depth of 31 km at station MACP is comparable to the ~ 34 km depth reported by Besana et al. (1995) based on RF beneath Tagaytay. In the SSM, crustal thickness corresponds to a large Late Cretaceous ophiolite near 15°N (Wolfe 1981). Magmatic episodes in this region occurred later, during the Paleocene–Eocene, compared to the NSM, which was active during the Cretaceous (Dimalanta and Yumul 2006). In southeastern Luzon, within the Bicol arc, station JCNP records a crustal thickness of 32 km. This crustal thickness in this region is attributed to the subduction of the northern margin of the Indo-Australian Plate beneath the Philippine Sea Plate, resulting in the formation of a magmatic arc (Dimalanta and Yumul 2006).

In Mindoro, particularly northward on Lubang island, we identified a relatively thin crust. Based on the northeasterly trend of aseismic characteristics, Lewis and Hayes (1989) attributed this to a slab tear caused by sharp bending in the Mindoro–Panay collision zone between approximately 14°N and 14.5°N. We observed thin crust in northwestern Mindoro, which is likely related to the pull-apart rifting of the Pleistocene Macolod Corridor. This rifting extends to the valley topography between Wawa and Mamburao Valley in northwestern Mindoro (Chen et al. 2015). Furthermore, the high *Vp/Vs* in this region may also correlate with slab tearing. Another possible explanation for the high *Vp/Vs* is anisotropy (Wang et al. 2012). A more comprehensive analysis of *Vp/Vs* and anisotropy could provide additional insight into the tectonic and geological framework of this region, though this falls beyond the scope of this study. We observed significant crustal thickening beneath station SANT, which may indicate the region where arc–continent collision occurred between the PCB and PMB (Yumul et al. 2009).

The crustal thickness estimation aligns with results obtained using gravity data by Parcutela et al. (2020). Gravity data indicate that the western segment of northern Luzon generally has a thicker crust than the eastern segment. It has been noted that the ophiolites exposed along the western side experienced higher rates of accretion compared to those on the eastern side. These lithospheric fragments, which accreted to the western part of the Philippines, are thought to have originated from a now-subducted proto-South China Sea. Additionally, gravity data corroborate the observation of thinner crust in northwestern Mindoro.

Conclusions

The autocorrelation of ambient noise combined with receiver function from 20 stations across the northern Philippines successfully identified the TWT of PmP waves. The corresponding crustal thickness, representing the Moho depth, was obtained by converting the TWT using the CRUST1.0 *P*-wave velocity model. The average Moho depth in Luzon and NW Mindoro is 29.45 ± 2.0 km and 25.58 ± 2.30 km, respectively. In Luzon, the western part features a thick crust, which thins toward the east. This crustal thinning is due to the limited contribution of magmatic processes in the eastern part of the island, as subduction along the Philippine Trench has only recently commenced. Slab tears were identified at 17°N and 14°N where the thinner crust was observed. In Mindoro, the region where microcontinental fragments collided with the Mindoro–Panay Islands exhibits a thick crust. In contrast, areas with thinner crust can be related to the extension of the Pleistocene Macolod Corridor rifting in Wawa and Mamburao.

Abbreviations

PMB Philippine mobile belt

PCB	Palawan Continental Block
MOR	Mid Oceanic Ridge
ACF	Autocorrelation function
IB	Ilocos Basin
CC	Cordillera Central
CB	Cagayan Basin
NSM	Northern Sierra Madre Range
ZOC	Zambales Ophiolite Complex
SSM	Southern Sierra Madre Range
CVST	Central Valley Suture
SPAC	Spatial autocorrelation
PHIVOLCS	Philippine Institute of Volcanology and Seismology
IES	Institute of Earth Science
NCU	National Central University
PWS	Phase-weighted stacking
TWT	Two-way traveltime
SNR	Signal-to-noise ratio
TRZ	Transverse–radial–vertical components

Supplementary Information

The online version contains supplementary material available at https://doi.org/10.1186/s40562-025-00420-7.

Supplementary Material 1.

Acknowledgements
We thank the two anonymous reviewers for constructive comments and suggestions. This work was supported by the Taiwan Earthquake Research Center (TEC) funded through the National Science and Technology Council (NSTC) of Taiwan with Grant Number 113-2923-M-008-005 and 113-2928-M-008-002. The TEC contribution number for this article is 00XXX.The maps were created using Generic Mapping Tools (Wessel and Smith 1998). The synthetic receiver functions for dipping Moho were created using *PyRaysum* (Bloch and Audet 2023) based on a ray theory-based code (Frederiksen and Bostock 2000)

Author contributions
EU: writing—original draft, visualization, methodology, investigation. PC: writing—review and editing, supervision, project administration, methodology, investigation, funding acquisition, data provider for NCU. BH: supervision, data provider for IES. C-NN: collect the teleseismic earthquake data for receiver function, investigation. TCB: collect the data from PHIVOLCS.

Funding
National Science and Technology Council (Taiwan).

Data availability
The dataset used during the current study is available from the corresponding author on reasonable request.

Declarations

Competing interests
The authors declare no competing interests.

Received: 20 March 2025 Accepted: 10 September 2025
Published online: 14 October 2025

References

Aki K (1957) Space and time spectra of stationary stochastic waves, with special reference to microtremors. Bull Earthquake Res Inst Univ Tokyo 35(3):415–456

Ammon CJ (1991) The isolation of receiver effects from teleseismic P waveforms. Bull Seismol Soc Am 81(6):2504–2510. https://doi.org/10.1785/bssa0810062504

Bai L, Tian X, Ritsema J (2010) Crustal structure beneath the Indochina peninsula from teleseismic receiver functions. Geophys Res Lett. https://doi.org/10.1029/2010gl044874

Bautista BC, Bautista MLP, Oike K, Wu FT, Punongbayan RS (2001) A new insight on the geometry of subducting slabs in northern Luzon, Philippines. Tectonophysics 339(3–4):279–310. https://doi.org/10.1016/s0040-1951(01)00120-2

Bellon H, Yumul GP Jr (2000) Mio-Pliocene magmatism in the Baguio Mining District (Luzon, Philippines): age clues to its geodynamic setting. Comptes Rendus De L Académie des Sciences - Series IIA - Earth and Planetary Science 331(4):295–302. https://doi.org/10.1016/s1251-8050(00)01415-4

Bensen GD, Ritzwoller MH, Barmin MP, Levshin AL, Lin F, Moschetti MP, Shapiro NM, Yang Y (2007) Processing seismic ambient noise data to obtain reliable broad-band surface wave dispersion measurements. Geophys J Int 169(3):1239–1260. https://doi.org/10.1111/j.1365-246x.2007.03374.x

Besana GM, Shibutani T, Hirano N, Ando M, Bautista B, Narag I, Punongbayan RS (1995) The shear wave velocity structure of the crust and uppermost mantle beneath Tagaytay, Philippines inferred from receiver function analysis. Geophys Res Lett 22(23):3143–3146. https://doi.org/10.1029/95gl03319

Bina CR, Čížková H, Chen P (2020) Evolution of subduction dip angles and seismic stress patterns during arc-continent collision: modeling Mindoro Island. Earth Planet Sci Lett 533:116054. https://doi.org/10.1016/j.epsl.2019.116054

Bloch W, Audet P (2023) PyRaysum: software for modeling ray-theoretical plane body-wave propagation in dipping anisotropic media. Seismica 2(1). https://doi.org/10.26443/seismica.v2i1.220

Cassidy JF (1992) Numerical experiments in broadband receiver function analysis. Bull Seismol Soc Am 82(3):1453–1474. https://doi.org/10.1785/bssa0820031453

Chen P, Olavere EA, Wang C, Bautista BC, Solidum RU, Liang W (2015) Seismotectonics of Mindoro, Philippines. Tectonophysics 640:70–79. https://doi.org/10.1016/j.tecto.2014.11.023

Claerbout JF (1968) Synthesis of a layered medium from its acoustic transmission response. Geophysics 33(2):264–269

Clayton RW, Wiggins RA (1976) Source shape estimation and deconvolution of teleseismic bodywaves. Geophys J Int 47(1):151–177. https://doi.org/10.1111/j.1365-246x.1976.tb01267.x

De Boer J, Odom LA, Ragland PC, Snider FG, Tilford NR (1980) The Bataan orogene: eastward subduction, tectonic rotations, and volcanism in the western Pacific (Philippines). Tectonophysics 67(3–4):251–282. https://doi.org/10.1016/0040-1951(80)90270-x

DeMets C, Gordon RG, Argus DF (2010) Geologically current plate motions. Geophys J Int 181(1):1–80. https://doi.org/10.1111/j.1365-246x.2009.04491.x

Dimalanta CB, Yumul GP (2003) Magmatic and amagmatic contributions to crustal growth of an Island-Arc system: the Philippine example. Int Geol Rev 45(10):922–935. https://doi.org/10.2747/0020-6814.45.10.922

Dimalanta C, Yumul G (2004) Crustal thickening in an active margin setting (Philippines): the whys and the hows. Episodes 27(4):260–264. https://doi.org/10.18814/epiiugs/2004/v27i4/004

Dimalanta CB, Yumul GP (2006) Magmatic and amagmatic contributions to crustal growth in the Philippine island arc system: comparison of the Cretaceous and post-Cretaceous periods. Geosci J 10(3):321–329. https://doi.org/10.1007/bf02910373

Fan J, Wu S, Spence G (2014) Tomographic evidence for a slab tear induced by fossil ridge subduction at Manila Trench, South China Sea. Int Geol Rev 57(5–8):998–1013. https://doi.org/10.1080/00206814.2014.929054

Fitch TJ (1972) Plate convergence, transcurrent faults, and internal deformation adjacent to Southeast Asia and the western Pacific. J Geophys Res Atmos 77(23):4432–4460. https://doi.org/10.1029/jb077i023p04432

Frederiksen AW, Bostock MG (2000) Modelling teleseismic waves in dipping anisotropic structures. Geophys J Int 141(2):401–412. https://doi.org/10.1046/j.1365-246x.2000.00090.x

Gómez-García C, Lebedev S, Meier T, Xu Y, Pape F, Wiesenberg L (2022) Ambient noise autocorrelation scheme for imaging the P-wave reflectivity of the lithosphere. Geophys J Int 233(3):1671–1693. https://doi.org/10.1093/gji/ggac509

Gorbatov A, Saygin E, Kennett BLN (2013) Crustal properties from seismic station autocorrelograms. Geophys J Int 192(2):861–870. https://doi.org/10.1093/gji/ggs064
Grad M, Tiira T (2009) The Moho depth map of the European Plate. Geophys J Int 176(1):279–292. https://doi.org/10.1111/j.1365-246x.2008.03919.x
Karig DE (1983) Accreted terranes in the northern part of the Philippine Archipelago. Tectonics 2(2):211–236. https://doi.org/10.1029/tc002i002p00211
Kennett B (2015) Lithosphere–asthenosphere P-wave reflectivity across Australia. Earth Planet Sci Lett 431:225–235. https://doi.org/10.1016/j.epsl.2015.09.039
Laske G, Masters G, Ma Z, Pasyanos M (2013) Update on CRUST1.0—a 1-degree global model of Earth's crust. Geophys Res Abstr 15:EGU2013-2658
Levin V, Park J (1997) P-sh conversions in a flat-layered medium with anisotropy of arbitrary orientation. Geophys J Int 131(2):253–266. https://doi.org/10.1111/j.1365-246x.1997.tb01220.x
Lewis SD, Hayes DE (1989) Plate convergence and deformation, North Luzon Ridge, Philippines. Tectonophysics 168(1–3):221–237. https://doi.org/10.1016/0040-1951(89)90377-6
Lombardi D, Braunmiller J, Kissling E, Giardini D (2008) Moho depth and Poisson's ratio in the Western-Central Alps from receiver functions. Geophys J Int 173(1):249–264. https://doi.org/10.1111/j.1365-246x.2007.03706.x
Manalo PC, Dimalanta CB, Faustino-Eslava DV, Ramos NT, Queaño KL, Yumul GP (2015) Crustal thickness variation from a continental to an island arc terrane: clues from the gravity signatures of the Central Philippines. J Asian Earth Sci 104:205–214. https://doi.org/10.1016/j.jseaes.2014.08.031
McCabe R, Almasco J, Diegor W (1982) Geologic and paleomagnetic evidence for a possible Miocene collision in western Panay, central Philippines. Geology 10(6):325. https://doi.org/10.1130/0091-7613(1982)10
Mroczek S, Tilmann F (2021) Joint ambient noise autocorrelation and receiver function analysis of the Moho. Geophys J Int 225(3):1920–1934. https://doi.org/10.1093/gji/ggab065
Nguyen C, Huang B, Lee T, Chen P, Nguyen VH, Narag IC, Bautista BC, Melosantos AA (2023) Slab tearing and lithospheric structures in Luzon island, Philippines: constraints from P- and S-wave local earthquake tomography. Front Earth Sci. https://doi.org/10.3389/feart.2023.1213498
Oren C, Nowack RL (2016) Seismic body-wave interferometry using noise autocorrelations for crustal structure. Geophys J Int 208(1):321–332. https://doi.org/10.1093/gji/ggw394
Parcutela NE, Dimalanta CB, Armada LT, Yumul GP (2020) PHILCRUST3.0: new constraints in crustal growth rate computations for the Philippine arc. J Asian Earth Sci X 4:100032. https://doi.org/10.1016/j.jaesx.2020.100032
Plank T, Langmuir CH (1998) The chemical composition of subducting sediment and its consequences for the crust and mantle. Chem Geol 145(3–4):325–394. https://doi.org/10.1016/s0009-2541(97)00150-2
Ruigrok E, Campman X, Wapenaar K (2011) Extraction of P-wave reflections from microseisms. C R Geosci 343(8–9):512–525. https://doi.org/10.1016/j.crte.2011.02.006
Savage MK (1998) Lower crustal anisotropy or dipping boundaries? Effects on receiver functions and a case study in New Zealand. J Geophys Res Atmos 103(B7):15069–15087. https://doi.org/10.1029/98jb00795
Schimmel M, Paulssen H (1997) Noise reduction and detection of weak, coherent signals through phase-weighted stacks. Geophys J Int 130(2):497–505. https://doi.org/10.1111/j.1365-246x.1997.tb05664.x
Snieder R, Miyazawa M, Slob E, Vasconcelos I, Wapenaar K (2009) A comparison of strategies for seismic interferometry. Surv Geophys 30(4–5):503–523. https://doi.org/10.1007/s10712-009-9069-z
Wang X, Schubnel A, Fortin J, David EC, Guéguen Y, Ge H (2012) High Vp/Vs ratio: saturated cracks or anisotropy effects? Geophys Res Lett. https://doi.org/10.1029/2012gl051742
Wapenaar K, Draganov D, Snieder R, Campman X, Verdel A (2010) Tutorial on seismic interferometry: Part 1 — basic principles and applications. Geophysics 75(5):75A195-75A209. https://doi.org/10.1190/1.3457445
Wessel P, Smith WHF (1998) New, improved version of the Generic Mapping Tools released. Eos Trans Am Geophys Union 79:579
Wolfe JA (1981) Philippine geochronology. J Geol Soc Philip 35:1–29
Xu M, He J (2022) SEISPy: python module for batch calculation and post-processing of receiver functions. Seismol Res Lett 94(2A):935–943. https://doi.org/10.1785/0220220288
Yumul GP Jr, Dimalanta CB, Marquez EJ, Queaño KL (2009) Onland signatures of the Palawan microcontinental block and Philippine mobile belt collision and crustal growth process: a review. J Asian Earth Sci 34(5):610–623. https://doi.org/10.1016/j.jseaes.2008.10.002
Zhang Y, Tian J, Hollings P, Gong L, Alburo I, Berador AE, Francisco DG, Li J, Chen H (2020) Mesozoic porphyry Cu–Au mineralization and associated adakite-like magmatism in the Philippines: insights from the giant Atlas deposit. Miner Deposita 55(5):881–900. https://doi.org/10.1007/s00126-019-00907-2
Zhu L, Kanamori H (2000) Moho depth variation in southern California from teleseismic receiver functions. J Geophys Res 105(B2):2969–2980. https://doi.org/10.1029/1999jb900322

Publisher's Note